Nearly automated motion artifacts correction between multi breath-hold short-axis and long-axis cine CMR images

Maria Chiara Carminati [a,*], Francesco Maffessanti [b], Enrico Gianluca Caiani [a]

[a] Dipartimento di Elettronica, Informazione e Bioingegneria, Politecnico di Milano, Milano, Italy
[b] Centro Cardiologico Monzino IRCSS, Milano, Italy

Article history:
Received 17 August 2013
Accepted 28 December 2013

1. Introduction

Cardiac magnetic resonance (CMR) imaging is the reference modality for non-invasive assessment of cardiac anatomy and function by computing ventricular volumes and mass. To this aim, the common protocol is based on the acquisition of cine MR images in the short-axis view (SA) from base to apex, from which endocardial and epicardial contours are fully or semi-automatically segmented and used to quantify ventricular function [1]. In the two-dimensional (2D) approach, endocardial and epicardial contours are combined from each SA plane and the ventricular volumes are computed using Simpson rule. The main limitation of this approach relies on the anisotropic resolution of the SA images, that are characterized by slice thickness up to 10 mm, together with base to apex motion of the ventricular chambers. The definition of the apex and, in particular, the valvular plane is therefore subjected to uncertainties, and the incorrect inclusion of a slice can introduce a bias in the mass and volume measurements. A possible way to overcome these limitations is related to the segmentation of endocardial and epicardial contours in a 3D space, in which the information available in SA and long-axis (LA) views have been combined [2–5]. The availability of a 3D dataset derived from the combination and interpolation of multiple 2D views allows the application of sophisticated semi-automated surface detection algorithms [6], thus resulting in faster analysis and more reproducible clinical parameters. Moreover, the extracted 3D endocardial and epicardial meshes can be utilized for patient-specific finite element modeling purposes [7].

However, in this context a pre-processing step appears mandatory to correct for possible misregistration artifacts due to the breathing-related motion during acquisition, before combining the available data into a 3D dataset. In fact, as each of the SA and LA dynamic images is acquired with ECG-triggering during different patient's apneas, the non-exact repeatability of breath-holding maneuver over all acquisitions could generate relative displacement between slices [8,9]. These artifacts are more prone to happen in heart failure patients, where the ability to maintain breath-hold is highly compromised.

Several studies have emphasized the importance of the correction of misregistration errors due to multiple breath-holds in cardiac MR [10,11,3,12], mandatory for 3D analysis, such as

* Corresponding author. Tel.: +39 02 2399 3322; fax: +39 02 2399 3397.
E-mail address: mariachiara.carminati@polimi.it (M.C. Carminati).

reconstruction of 3D datasets [13], 3D reconstruction of shape and deformation of the heart [2,14] and fusion with other imaging modalities [15,11,16–18]. Automated or semi-automated correction methods have been proposed and different approaches have been used featuring in-plane correction [17,15,19] or both in-plane and out-of-plane corrections [10,20,13,21,12,22]. We hypothesized that an efficient and nearly automated correction method for compensating in-plane movement artifacts, without the need of additional CMR sequence acquisition, could be applied to standard cine SA and two- and four-chamber (2CH 4CH) LA images, as a pre-processing step for 3D volumetric analysis.

Accordingly, our aims were (1) to develop a fast and automated misalignment correction method between different slices in SA images, on the basis of their similarity at intersections with the LA images, without the need of *a priori* segmentation or ROI definition, (2) to validate its performance on a virtual phantom dataset created ad hoc from an high resolution cardiac computed tomography (CT) frame in which known relative movements were applied, (3) to test its efficacy when applied to real CMR data obtained in consecutive patients by visual comparison of corrected and non-corrected datasets.

2. Methods

2.1. 3D representation

The algorithm was developed using the VTK open source visualization toolkit [23] and Grassroots DICOM (GDCM) library for DICOM handling [24].

Each 2D image is represented in the 3D space as an oriented array, whose geometrical characteristics were calculated from the information stored in the header of the DICOM file. In particular, three points (origin and two more points) are necessary to define the plane position and orientation and are calculated as follows:

$$\begin{aligned} &Origin = IPP \\ &\text{Point1} = \text{Origin} + \text{IOP} * \text{axis1} \\ &\text{Point2} = \text{Origin} + \text{IOP} * \text{axis2} \end{aligned} \quad (1)$$

where IPP is the image position patient, IOP is the image orientation patient, axis1 and axis2 take into account the size of each image. The image data is then passed to the rendering scene as a texture map associated to the corresponding plane.

2.2. Long-axis correction

Prior to SA image position correction, LA 2CH and 4CH images alignment was visually checked in the 3D space and manually adjusted if necessary. Manual correction was applied in the form of a 3D translation by moving the 2CH image in the rendering scene until the correct matching with the 4CH image was reached. This first step was performed manually due to the lack of adequate spatial information at the 2CH–4CH intersection.

2.3. Short-axis correction

The proposed method for motion artifacts compensation is based on the maximization of the correlation of pixel intensities along the intersections between each SA and the LA 2CH and 4CH planes. The resulting correction is a translation, 2 degrees of freedom (dof) transformation, along the image plane.

First, the line in the 3D space representing the intersection between each SA and each LA image is computed (Fig. 1, top panel); then, the corresponding intensity profiles are extracted separately from the SA and the LA image, using linear interpolation, thus resulting in two 1D signals (Fig. 1, bottom left panel).

These signals represent the input of a cost function that guides the correction, based on the normalized cross-correlation (NCC) on the hypothesis that the two intensity profiles are expected to be equal once the images are properly aligned.

NCC was computed as follows:

$$\mathrm{NCC}(d) = \frac{\sum_i [(x_i - m_x)(y_{i-d} - m_y)]}{\sqrt{\sum_i (x_i - m_x)^2}\ \sqrt{\sum_i (y_{i-d} - m_y)^2}} \quad (2)$$

where x_i and y_i are the two 1D series of pixel values to be correlated, m_x and m_y are their corresponding mean values, and d is the lag of the cross-correlation.

The search domain for the optimal position of the SA image, defining the range of values of d, was defined as a neighborhood of ± 10 pixels around the original SA plane position, defined by the IPP and decomposed in the x- and y-image directions. The neighborhood size was set by considering the pixel spacing in order to be able to capture potential misalignments of the order of ± 1.5 cm.

Starting from the original position, each SA image was shifted using a one-pixel step length within the search domain and intensity profile values at SA-LA 2CH and at SA-LA 4CH intersections were obtained and $\mathrm{NCC}_{\mathrm{SA-2CH}}$ and $\mathrm{NCC}_{\mathrm{SA-4CH}}$ were computed (Fig. 1, bottom mid panel). To compose the results obtained considering separately the LA views, the mean NCC was computed as follows:

$$\mathrm{mNCC} = \frac{(\mathrm{NCC}_{\mathrm{SA-2CH}} + \mathrm{NCC}_{\mathrm{SA-4CH}})}{2} \quad (3)$$

Finally, the optimal correction was defined as the 2D displacement featuring the maximum of mNCC (Fig. 1, bottom panel right), and applied to the SA image.

Each SA image was corrected independently from the others and a specific system of reference was defined with the origin corresponding to the IPP and the x- and y-axis corresponding to the x- and y-image directions, respectively, according to the IOP. Consequently, the z-axis was coincident to the left ventricular (LV) long-axis, thus resulting in a plane-specific reference system.

3. Validation

3.1. CT dataset

A high resolution cardiac CT 3D dataset (GE Medical System, $512 \times 512 \times 399$ voxels with spacing $0.51 \times 0.51 \times 0.625$ mm^3) of a patient with cardiac dyssynchrony was used to apply known misalignments to selected 2D slices for testing the algorithm performance, even if with different ranges of videointensity with respect to the MR data. In particular, 6 cut-planes corresponding to 2CH, 4CH and 3CH LA and 3 SA (at basal, mid and apical level) views were selected. From the same patient, also CMR was available (GE, 1.5 T, matrix dimension 512×512, spacing 0.74×0.74 mm^2, slice thickness 8 mm). To ensure temporal correspondence, a frame was chosen in both MR and CT datasets at 40% of the cardiac cycle (60 bpm for both).

The choice to use a 3D cardiac CT frame was driven by the fact that no high resolution MR volume or perfectly aligned MR dataset was available in our study.

In particular, the 6 cut-planes were extracted from the CT dataset in order to:

- test the algorithm performance by comparison of the resulting correction with known misalignments applied to SA planes at different levels of the ventricle;
- evaluate the additional benefit of including the LA 3CH view, together with LA 2CH and 4CH views.

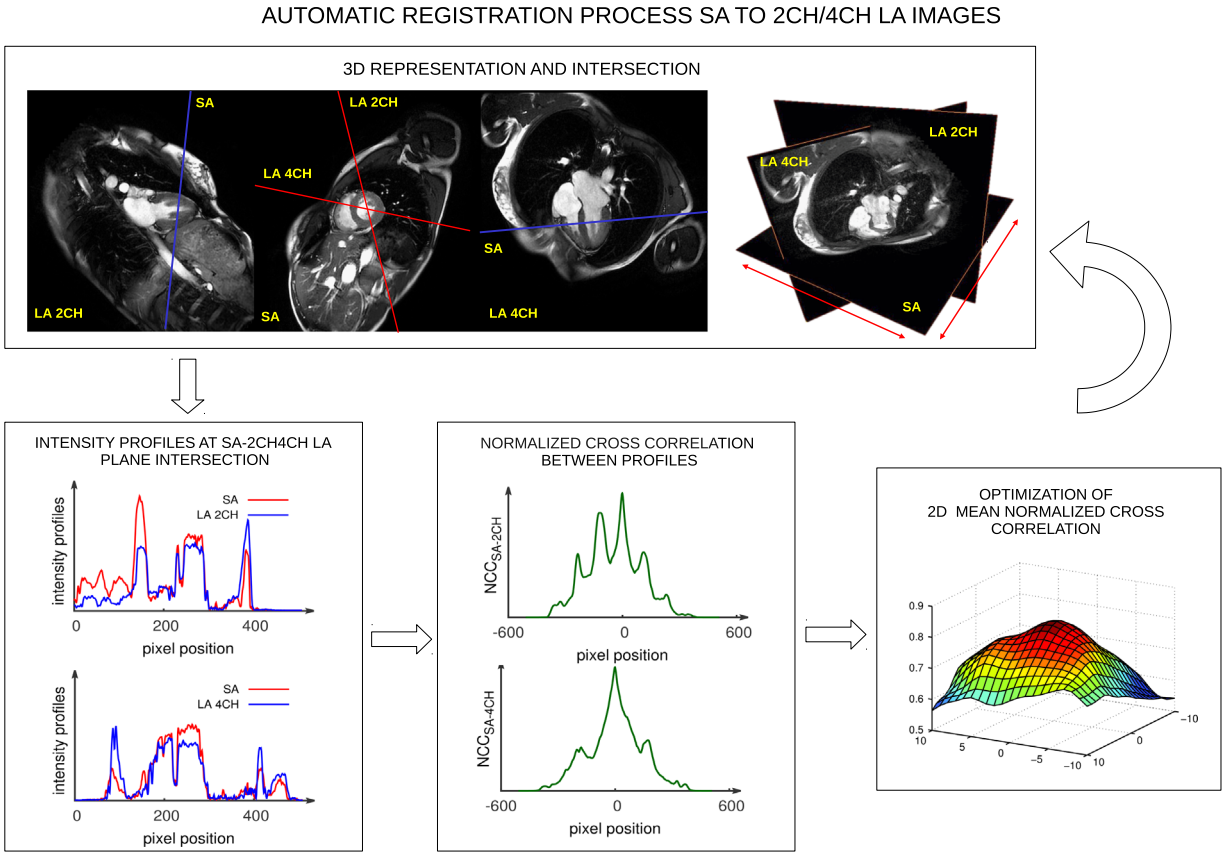

Fig. 1. Automatic registration process.

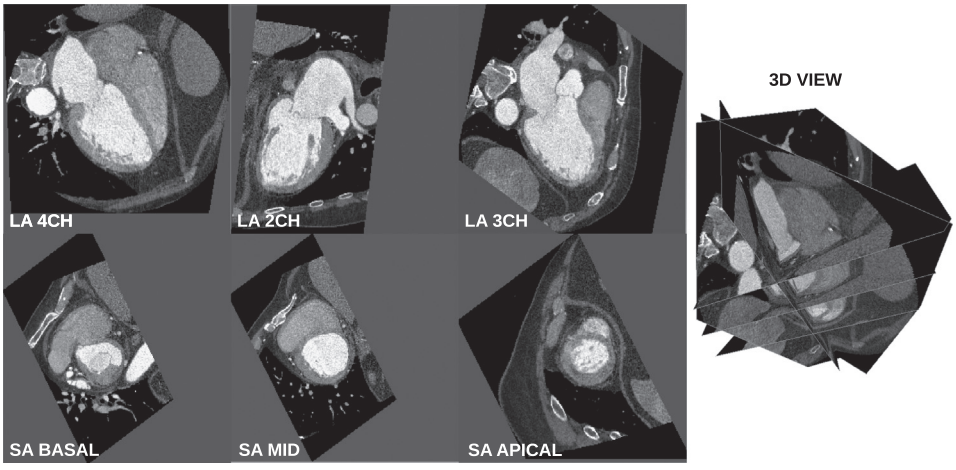

Fig. 2. LA and SA projections extracted from CT after CT-MR rigid registration.

In order to extract the 6 cut-planes by simulating the orientation of the corresponding 2D planes acquired in a clinical MRI protocol, rigid registration (6 dof) between the CT frame and the MRI SA stack was applied. First, a 3D MRI volume was obtained from the SA stack. The completely automated registration framework was developed using the open source ITK library [25] and consisted of two consecutive steps. First, the reciprocal position of the two stacks was adjusted by overlying the geometrical center of the bounding boxes. This operation provided a 3D translation to be applied to the moving image prior to registration.

In the second step, a multi-resolution 3D to 3D voxel-based rigid registration approach was adopted, with normalized mutual information metric and gradient descent optimizer [26]. Two levels of multi-resolution were defined with isotropic subsampling grid equal to [4, 4, 4] and [2, 2, 2], while the finest resolution (i.e., [1, 1, 1]) was omitted in order to reduce computational time. Also, as the CT volume has higher spatial resolution than the MR volume, the latter was set as fixed in order to minimize the computational time required by the resampling process of the moving image on the fixed image at every step of the registration. The registered data was visually inspected and judged reliable for correspondence of cardiac structures.

The retrieved coordinates transformation was applied to each SA and 2CH–3CH–4CH LA direction cosines (T_{SA}, T_{2CH}, T_{3CH} and T_{4CH}) and

image position patient to obtain plane orientations for plane extraction on the CT frame:

$$T_{SA-CT} = T_{SA} \times T_{MR}^{CT}$$
$$T_{2CH-CT} = T_{2CH} \times T_{MR}^{CT}$$
$$T_{3CH-CT} = T_{3CH} \times T_{MR}^{CT}$$
$$T_{4CH-CT} = T_{4CH} \times T_{MR}^{CT} \quad (4)$$

where T_{MR}^{CT} is the 4×4 transformation matrix resulting from the rigid registration, T_{2CH-CT}, T_{3CH-CT}, T_{4CH-CT} and T_{SA-CT} represent the final cutting planes used to recreate LA and SA slices from CT data.

Fig. 2 shows the resulting CT dataset used for the validation, constituted by 6 planes, 3 in the LA view (LA_{CT}) and 3 in the SA view (SA_{CT}), that represents the gold standard positions of each plane.

3.1.1. Simulations

The simulated displacements of the SA_{CT} images with respect to their gold standard position were achieved by in-plane translation in x- and y-directions in the range ± 10 pixels (corresponding to ± 5.1 mm). By uniformly sampling this continuous range every 0.5 pixel (equal to 0.255 mm), a grid of 1681 points representing the possible displacements was obtained. A set of 100 points, representing the simulated displacements, was randomly selected from the grid, to determine the 2D translation to be applied to each SA_{CT} image. To evaluate polarization of the residual error due to the utilized sampling grid, an additive white Gaussian noise characterized by SNR of 20 dB was consequently applied to the point coordinates. The resulting distribution of displacements was characterized by values of 3.95 ± 3.26 mm (mean $\pm$ 2std).

3.1.2. Error estimate

The performance of the registration algorithm (see Section 2.3) was assessed in terms of residual error between the corrected and the gold standard position of each SA_{CT} image as follows:

$$err_i = \sqrt{(\delta x_i - \delta x_i')^2 + (\delta y_i - \delta y_i')^2}, \quad i = 1, \ldots, N \quad (5)$$

where δx_i and δy_i are the known displacements applied to the SA_{CT} image, $\delta x_i'$ and $\delta y_i'$ are, respectively, the computed corrections along the x- and the y-axis of the SA_{CT} plane for the ith simulated displacement and finally $N = 100$ is total number of simulations described in the previous section.

To evaluate the potential benefit of using an additional LA view to guide registration of the SA_{CT}, two different registration metrics were considered: the one described in Eq. (3) and its modification including the information from the 3CH view:

$$\text{mNCC} = \frac{(NCC_{SA-2CH} + NCC_{SA-4CH} + NCC_{SA-3CH})}{3} \quad (6)$$

where NCC_{SA-2CH}, NCC_{SA-4CH} and NCC_{SA-3CH} are the NCC values computed between intensity profiles at intersections between SA and LA in 2CH, 4CH and 3CH views, respectively.

3.1.3. Results of simulations

Fig. 3 shows the residual errors after correction using the metric based on 2 or 3LA views (Eqs. (3) and (6), respectively). All median errors were found lower than CT pixel resolution (0.51 mm) and detailed values are reported in Table 1. Nonparametric statistical analysis was performed to compare the distribution of residual errors obtained from the simulation process. In particular, Wilcoxon signed rank test was applied to test for differences using 2LA or 3LA in the registration process: a statistically significant reduction in error using 3LA was found at the apical level (percentage error reduction of 2.15%). This improvement was obtained with an increase in computational time of 0.62 s, corresponding to +47% of the mean time required to register a single SA image (1.33 s) using 2LA.

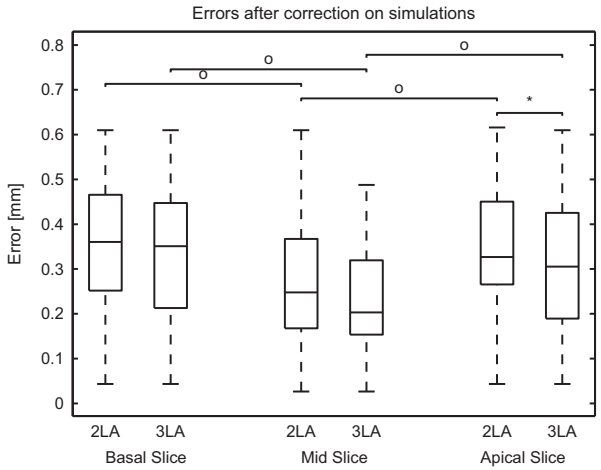

Fig. 3. Box–whisker plots of residual error after correction (outliers, +) on simulated displacement , *: $p < .05$ Wilcoxon signed rank test 2LA vs 3LA; Kruskal Wallis, °: $p < .05$ vs mid.

Table 1
Errors on CT dataset simulation.

Error in simulation median value (interquartile range) (mm)		
Basal	Mid	Apical
0.36 (0.21)°	0.25 (0.19)	0.33 (0.18)°
0.35 (0.23)°	0.20 (0.17)	0.30 (0.24)*,°

* $p < .05$ Wilcoxon signed rank test 2LA vs 3LA.
° $p < .05$ Kruskal Wallis vs mid.

Kruskal Wallis statistics was applied to evaluate registration performance dependency from slice location along the ventricle: a reduced error in the mid slice was found compared to basal and apical ones for both 2LA and 3LA.

These results showed that the introduction of the 3CH LA view generated a limited benefit in terms of error reduction with a noticeable increase in computational time, for that reason we chose to exclude the 3CH LA view from further clinical MR data evaluation.

3.2. Clinical MR data evaluation

Twenty consecutive patients, evaluated at the Centro Cardiologico Monzino and referred for cardiac MRI, were studied (2 patients with normal LV function, 11 with previous myocardial infarction, 4 with wall motion dyssynchrony, 1 with dilated cardiomyopathy, 1 with thalassemia and 1 with severe pulmonary hypertension). All patients were in sinus rhythm during image acquisition, and each of them gave his/her informed consent to the study. ECG-gated, steady-state free precession (SSFP) cine-images (GE, 1.5 T, matrix dimension 512×512 and spacing 0.74×0.74 mm, or matrix dimension 256×256 and spacing 1.56×1.56 mm, slice thickness 8 mm) were acquired in SA (from atrium to apex) and in LA 2CH and 4CH views.

The following analysis was performed in order to test the algorithm performance on real clinical data: in the end-diastolic (ED) and end-systolic (ES) frames, first, the 2CH and 4CH LA were manually aligned, if needed, as described in Section 2.2. Then, as no ground truth was available, two experienced observers (OBS_1, OBS_2) were asked to independently visualize the 3D view corresponding to the intersecting 2CH–4CH LA with each of the SA planes, from the left atrium to the LV apex. The original data

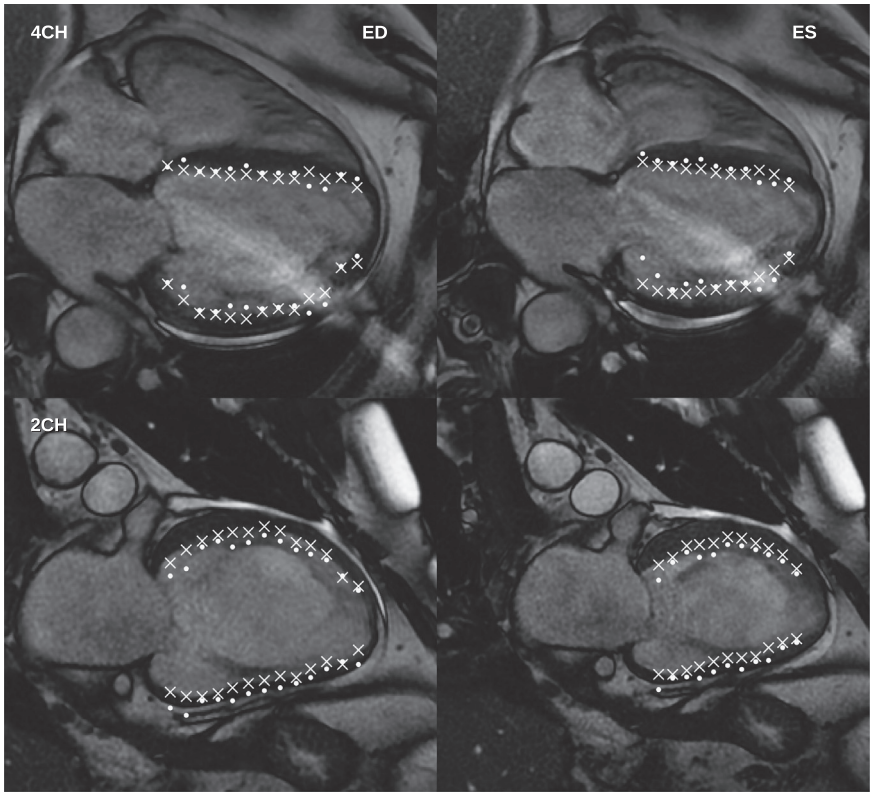

Fig. 4. Example of the quantitative validation in one ED (left panels) and ES (right panels) frames: intersections before (·) and after correction (×) of the LV endocardial contours manually traced on SA images with the LA 4CH (top panels) and 2CH (bottom panels) LA planes, from which residual errors were computed as the distances to the LA endocardial contours (not shown for clarity).

(without motion correction) was randomly visualized on one half of the screen, while the corrected data was on the other half. Visualization controls (zoom and camera position) were automatically applied on both half-screens to guarantee the same orientation and scale of the images to be compared.

The observers were asked to evaluate the correspondence between each SA and 2CH–4CH LA, in terms of left atrial and ventricular endocardial contours matching, by ranking it with the following scores:

- 0: no difference between the two half screens;
- 1: improvement assigned to one half screen.

For each observer, the algorithm performance was evaluated by counting the number of SA planes in which

- the correction did not generate any visual improvement (i.e., score 0);
- the correction generated an improvement (i.e., score 1 assigned to the corrected half screen, $+$);
- the correction generated further misalignment (i.e., score 1 assigned to the non corrected half screen, $-$).

The range of the applied shifts was computed both globally and for each group (0, $+$, $-$). The inter-observer variability was evaluated by considering the concordant and discordant scores assigned by the two observers on the same SA, and statistical significance was tested by Cohen's kappa analysis.

In addition, a quantitative validation was carried out by considering the distances before and after correction between LA and SA endocardial LV contours manually delineated by a trained observer. This analysis was performed on the SA slices containing the LV only. Residual positional offsets were quantified as the distance along the SA–LA plane intersection between the traced endocardial contour on each SA image and that delineated on the 2CH and 4CH LA images, respectively (see Fig. 4). Wilcoxon signed rank test was applied to test for the significance of the improvement of endocardial matching due to the applied correction. Furthermore, in order to evaluate the effect of observer subjectivity of contour manual tracing, the following analysis was performed: the same observer (OBS_1) was asked to blindly repeat the LV endocardial manual contouring in the ED and ES frames on a subgroup of 10 patients randomly chosen, while the 10 remaining patients were manually analyzed by a second blind and independent observer (OBS_2). Residual offset between SA and LA contours after image correction was computed and tested for inter- and intra-observer variability by linear correlation and Bland–Altman method [33]. Wilcoxon signed rank test was used to test whether the systematic error was statistically significant different from zero (*, $p < .05$). The coefficient of variability (CoV) was calculated as the standard deviation of the signed difference between the two sets of measurements divided by the mean value of the considered parameter.

3.2.1. Results

The manual alignment of 2CH–4CH LA planes was necessary in 19/40 images, requiring about 2 min each, with an applied correction in the range 0–16.31 mm. An example of such correction is presented in Fig. 5, where the original misalignment along the intersection is noticeable in particular at the apex and at the chest.

The automatic correction of SA was applied to a total number of 542 SA images, with an average processing time of 0.5 s on a general purpose laptop, with an applied correction in the range of 0–13.45 mm (0–10.81 mm for SA corresponding to the atrium and

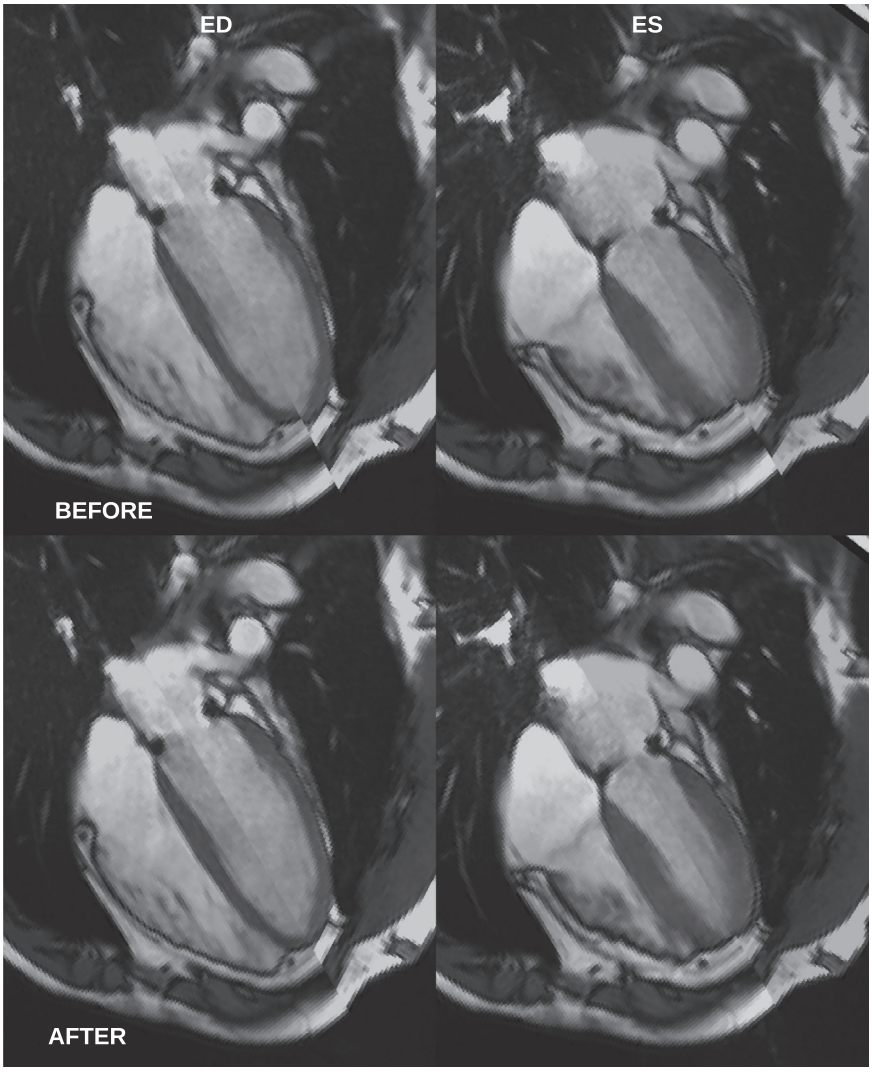

Fig. 5. Example of manual correction of LA 2CH plane in ED (left panels) and ES (right panels) frames: 2CH LA image is shifted from its original position (top) in order to improve the correspondence at the intersection with the 4CH view (bottom).

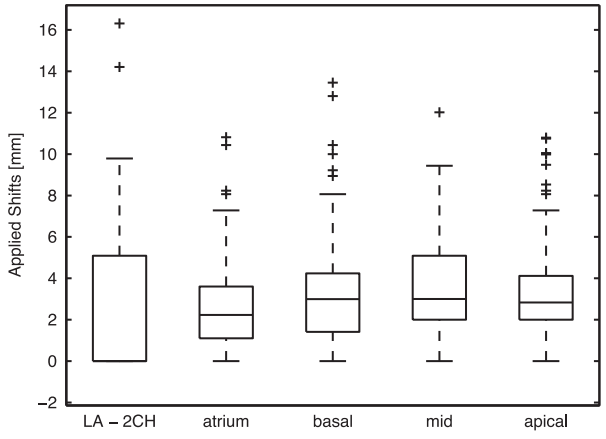

Fig. 6. Ranges of applied shifts: LA 2CH view, SA atrial, basal, mid and apical LV slices.

0–13.45 mm, 0–12.02 mm, 0–10.79 mm, for SA corresponding to the basal, mid and apical LVs). We found a lower computational time compared to those found during simulation, due to the lower spatial resolution of the CMR data with respect to the CT dataset.

In Fig. 6 the distributions of the applied corrections are reported as box–whisker plots.

In Table 2, the results of the two observers visual assessment are shown. The applied correction was found to generate an improvement for both observers in $>40\%$ of the analyzed images, while the visual perception did not change in about 45%. In the remaining images, the correction resulted in increased misalignment. The results of the inter-observer variability analysis are also presented in Table 2: in 67.71% of the images, agreement between the observers was achieved. The majority of the disagreement (21.76%) was found associated to the pair of scores 0 vs $+$, on the contrary, the disagreement related to a completely opposite interpretation $+$ vs $-$ was 2.95%, while 0 vs $-$ resulted in 7.57%. Linear weighted Cohen's kappa analysis verified the significance of the observed agreement showing kappa value of 0.44.

It is worth noting that in $>85\%$ (223/251 for OBS_1, 213/248 for OBS_2) of images classified with score 0, only a minimal shift of maximum 2 pixels per direction was applied by the algorithm, while images classified by both observers as worsened were characterized by a larger displacement (Fig. 8). However, in some outliers, images classified with score 0 were characterized by greater values of correction applied (>8 mm), thus showing potential limitation in the visual assessment due to subjective perception.

Table 2
Top: observer grading, absolute number of slices (correspondent percentage) assigned to class 0, + or − by the two observers. Bottom: inter-observer agreement, absolute number of slices (correspondent percentage).

Observer	0	+	−
OBS_1	251 (46.31%)	229 (42.25%)	62 (11.44%)
OBS_2	248 (45.76%)	223 (41.14%)	71 (13.1%)
OBS_1–OBS_2	0	+	−
0	170 (31.36%)	57 (10.51%)	21 (3.87%)
+	61 (11.25%)	159 (29.33%)	3 (0.55%)
−	20 (3.7%)	13 (2.4%)	38 (7.01%)

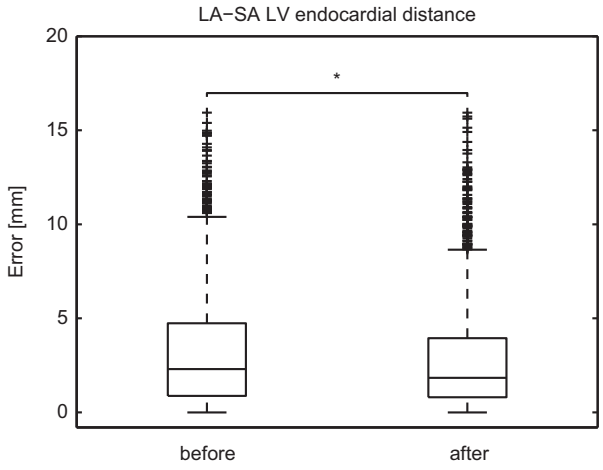

Fig. 7. Distances between LA (2CH and 4CH) and SA LV endocardial contours before and after correction, $p < .05$ Wilcoxon signed rank test.

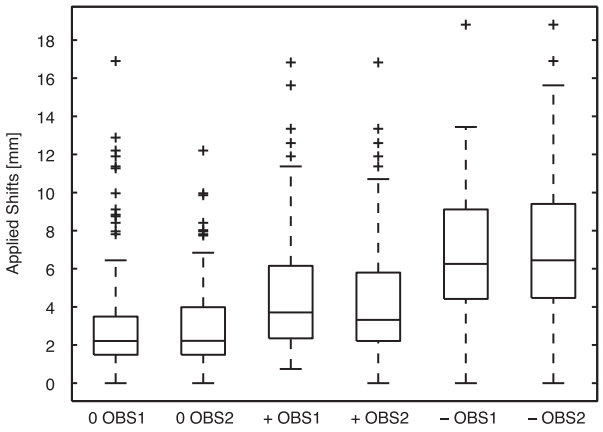

Fig. 8. Range of correction classified by score given by each observer.

Residual errors after correction computed as distances between LA and SA LV endocardial contours are reported as box–whisker plots (Fig. 7) and significant reduction of the residual offset was found (median (25th; 75th percentile): 2.4 mm (0.88; 4.74) before correction vs 1.8 mm (0.80; 3.95) after correction).

To appreciate the effectiveness of the applied alignment, in Fig. 9 a 3D view of the same dataset in ED and ES frames before and after the application of the misalignment correction is presented.

Inter- and intra-observer analysis of residual error after correction showed significant correlation coefficients (R) of 0.84 and 0.78, respectively, with minimal biases and narrow limits of agreement (inter: 0.174* (−2.91; 3.2) mm; intra: 0.173 (−5.2; 5.6) mm). In both cases, small CoVs of residual error were found (inter: 0.64%; intra: 0.74%), proving the repeatability of the proposed quantitative validation.

4. Discussion

We proposed a nearly automated and unsupervised method for correcting in-plane misalignment of SA images based on the similarity of intensities at LA intersections.

Compared to other methods recently proposed in the literature, our approach is based on voxel intensities and does not rely on LV manual segmentation [13,3], thus resulting in more efficient and not operator dependent results. In contrast to [20,5] or [27,28,15], where 3D to 3D or slice to volume registration approaches were, respectively, applied, we used datasets acquired in the clinical routine (SA and 2CH–4CH free precession images, similar to [12,22,10]), to avoid the acquisition of additional sequences, that impact exam duration and patient comfort

Our method compensates for translational but not rotational artifacts. This choice was made because, as recently reported in the literature [8], the rigid body motion of the heart due to respiration is mainly a translation in the cranio-caudal direction, while very limited rotations (typically a couple of degrees) are reported, so that they can be considered as minor artifacts and therefore neglected in first instance. In other studies [10,12], rotational correction has been handled. In Slomka et al., out of plane tilt was considered and they validated the method performance against manual correction performed by two observers. However, they were not able to validate for such rotational correction, because the observers did not attempt to adjust the tilt of SA plane as no obvious tilt was visible in the images. In Elen et al., a method for full 3-D translations and rotations correction is presented; however, no significant improvement on final results with the rotational correction was found.

Both [12] and [10] correct for misalignment by considering all frames belonging to a single acquisition, thus applying the same correction to each SA plane in all cine phases. In our approach, instead, each frame and each SA image are handled independently, in order to correct also for little movement that could occur during apnea resulting in relative shifts in the same image plane in different cine phases. A single frame approach for compensating breath hold artifacts in late gadolinium enhanced CMR is also presented in [22], where a new cost term for preserving anatomical continuity of the heart is introduced, however no validation study on misalignment correction is presented. Unlike other authors, we chose the NCC as metric to drive the alignment correction, as SA and LA images are expected to be characterized by similar value of intensities, and the cross-correlation is normalized in order to compensate for possible differences in intensity scale [29]. This assumption could be source of inaccuracies in the presence of inhomogeneity of the MR field, resulting in lower similarity of intensities in different projections. However, recent advances in MR hardware improved magnetic field homogeneity in SSFP images, thus resulting in images with limited inhomogeneity artifacts [30–32].

To the best of our knowledge, the method that we are presenting is the fastest among those already published in the literature using the same CMR images [22,12,10], and therefore is potentially easier to be integrated in a clinical environment. Its complexity is similar to [12], where in-plane correction is handled, but lower than [22] and [10] in which 3D translation and 3D translation and rotation are, respectively, proposed. Furthermore, it does not rely on patient-specific ROI definition of the cardiac

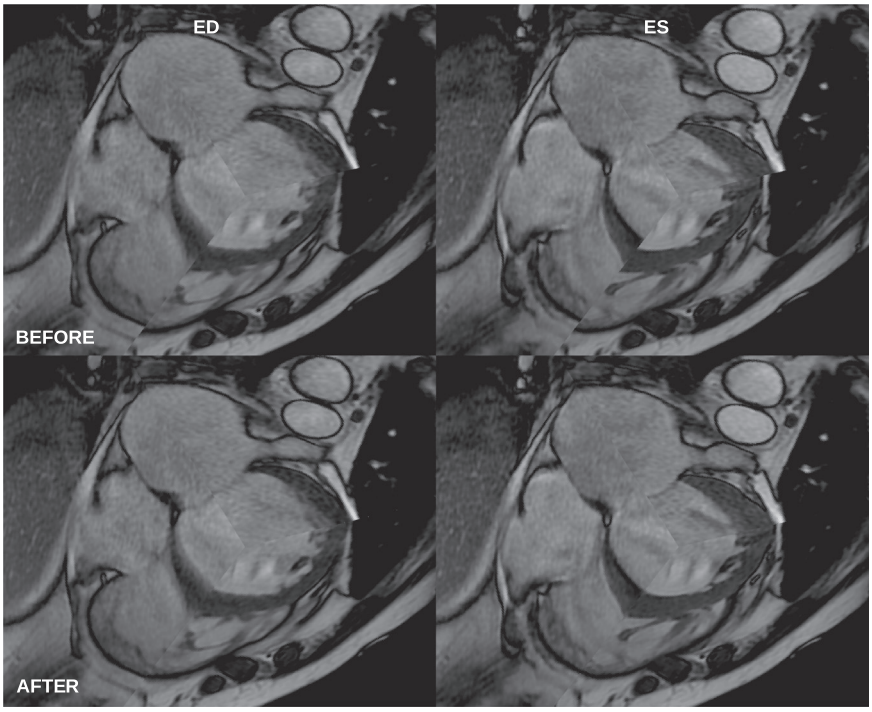

Fig. 9. Example of automatic correction of SA plane in ED and ES frames.

structures [10,22], thus resulting in a more automated approach. In fact, we consider that differences in lung volumes during image acquisition cause displacements in cardiac structures and also in other thoracic areas. This is particularly noticeable in correspondence with the fat and skin of the thorax, which appears brighter in free precession images. When extracting intensity profiles at SA and LA intersections the brighter voxels corresponding to these areas contribute to the calculation of the NCC and thus help driving the correction.

A first validation of the algorithm was based on a dataset created ad hoc from a CT frame, which allowed to have high-resolution data with known ground truth position. Accuracy of the misalignment corrections resulted in values of the order of the pixel resolution, which is comparable with other methods [12,20,10]. Higher accuracy was found for the mid slice, compared to the apical and basal ones, probably due to the larger informative contribution at this ventricular level. In the CT dataset it was also possible to test the additional use of the 3CH LA image together with the 2CH and 4CH LA, which is often acquired in the clinical routine, but significant improvement in algorithm performance was found only on the apical slice at expenses of longer computational time. However, the presented method is expandable to a custom number of LA images (including 3CH or radial views), thus potentially obtaining more accurate results.

The algorithm application to CMR datasets showed that the correction was needed in more than 50% of all processed slices and at least in one slice for each patient, confirming that breath-holds misalignment is common artifacts in CMR images, as reported in previous studies [12,10,3,22,21]. In particular, such corrections appear then mandatory when 2D CMR slices are combined in the 3D space for LV segmentation or modeling purposes. The algorithm showed a valuable improvement, measured as visual perception of two experienced observers, in about 70% of the SA images in need for correction of the CMR datasets, proving the reliability and utility of the proposed approach. However, in about 13% of all cases, misalignments worsened after algorithm's application and higher values of correction were applied. In these cases, more complex misalignments probably occurred, and approaches including 3D translational and rotational corrections should be considered. The method itself in its present form is not able to automatically detect failure cases and visual inspection after correction is needed to examine images and possibly refuse proposed corrections. In this respect, a possible strategy could be to limit this step only to the images where a certain correction displacement is considered at risk of failure. By observing from our visual results that failure cases for both OBS_1 and OBS_2 were characterized by significantly higher range of corrections (median value of 6.25 mm and 6.44 mm, respectively) compared to success cases, a basic implementation of this strategy would be to show a warning message if the absolute value of the proposed correction is higher than 6 mm. It should be noticed that our approach is not intended to be applied unsupervised on RAW image data after acquisition, but it is proposed as an off-line procedure to be applied when 3D analysis approach (segmentation, fusion with other imaging modalities) is required, in particular for patient specific modeling purposes.

A first qualitative validation was performed visually by two experienced observers, as no ground truth was available for the CMR datasets; however, a moderate kappa coefficient was found (0.44) as a result of inter-observer variability in the interpretation.

An additional quantitative validation protocol, based on the distances between LA and SA LV manual endocardial contours, was performed in order to measure the residual error of relative slice position in both ED and ES frames. The method was capable to reduce the median error from 2.4 mm (before) to 1.8 mm (after correction). These results are supported by intra- and inter-observer variability analysis that was characterized by very limited CoVs. Our findings are consistent with variability analysis previously reported in the literature [34,35], in which repeatability of ventricular volume and mass measures was tested, thus proving the effective reduction in misalignments regardless of the intrinsic variability of the utilized gold standard (manual tracing).

The proposed method presents some limitations. First, it does not correct all possible misalignments, i.e., 3D translations and rotations, but it focuses on the correction of the most obvious 2D translational artifacts. We decided to neglect out-of-plane

translation of SA slices and to maintain image planes equally spaced. As a matter of fact, we focused on the correction of the most obvious 2D translational artifacts, in order to prevent the increase of computational burden, allowing to obtain a quick and efficient tool to be applied as an off-line post processing step after routine image acquisition.

Furthermore, the validation was performed from a cardiac CT frame which allows for high resolution reconstructed SA and LA images with known gold standard position, but it is characterized by different intensity values, as well as different contrast to noise ratios, compared to the CMR data. However, it may represent a good surrogate dataset for validation purposes, since the algorithm is proposed to work on images acquired in different plane orientations using the same modality, independent from their intensities. The validation protocol of the CT dataset was designed to assess the algorithm performance under the hypothesis of planar misregistration errors. Following this scheme, the applied simulations did not take into account for more general motion.

Finally, 2CH and 4CH LA registration steps were manual due to the poor information that can be extracted at 2CH and 4CH LA intersections.

In conclusion, motion artifacts in multi breath-hold cine CMR images can be efficiently corrected off-line after standard image acquisition with a fast and nearly automated method. The proposed approach allows for correct 3D visualization of SA and LA images and represents the necessary pre-processing step for 3D analysis as surface extraction, LV modeling and fusion with other imaging modalities.

Conflict of interest statement

None declared.

References

[1] C. Petitjean, J.-N. Dacher, A review of segmentation methods in short axis cardiac MR images, Med. Image Anal. 15 (2) (2011) 169–184.

[2] J.M. Lötjönen, V.M. Järvinen, B. Cheong, E. Wu, S. Kivistö, et al., Evaluation of cardiac biventricular segmentation from multiaxis MRI data: a multicenter study, J. Magn. Reson. Imaging 28 (3) (2008) 626–636.

[3] H.C. Van Assen, M.G. Danilouchkine, A.F. Frangi, S. Ordás, J.J. Westenberg, J.H. Reiber, B.P. Lelieveldt, SPASM: a 3D-ASM for segmentation of sparse and arbitrarily oriented cardiac MRI data, Med. Image Anal. 10 (2) (2006) 286–303.

[4] D. Saring, J. Relan, M. Groth, K. Mullerleile, H. Handels, 3D segmentation of the left ventricle combining long-and short-axis MR images, Methods Inf. Med. 48 (4) (2009) 340.

[5] S. Ur Rahman, S. Wesarg, Upsampling of cardiac MR images: comparison of averaging and super-resolution for the combination of multiple views, in: 10th IEEE International Conference on Information Technology and Applications in Biomedicine (ITAB), 2010, IEEE, 2010, pp. 1–4.

[6] C. Corsi, C. Lamberti, O. Catalano, P. MacEneaney, D. Bardo, R.M. Lang, E.G. Caiani, V. Mor-Avi, Improved quantification of left ventricular volumes and mass based on endocardial and epicardial surface detection from cardiac mr images using level set models, J. Cardiovasc. Magn. Reson. 7 (3) (2005) 595–602.

[7] C. Conti, E. Votta, C. Corsi, D. De Marchi, G. Tarroni, M. Stevanella, M. Lombardi, O. Parodi, E. Caiani, A. Redaelli, Left ventricular modelling: a quantitative functional assessment tool based on cardiac magnetic resonance imaging, Interface Focus 1 (3) (2011) 384–395.

[8] K. McLeish, D.L.G. Hill, D. Atkinson, J.M. Blackall, R. Razavi, A study of the motion and deformation of the heart due to respiration, IEEE Trans. Med. Imaging 21 (9) (2002) 1142–1150.

[9] A.D. Scott, J. Keegan, D.N. Firmin, Motion in cardiovascular MR imaging, Radiology 250 (2) (2009) 331–351.

[10] A. Elen, J. Hermans, J. Ganame, D. Loeckx, J. Bogaert, F. Maes, P. Suetens, Automatic 3-D breath-hold related motion correction of dynamic multislice MRI, IEEE Trans. Med. Imaging 29 (3) (2010) 868–878.

[11] L. Cordero-Grande, S. Merino-Caviedes, X. Alba, R. Figueras i Ventura, A. Frangi, C. Alberola-Lopez, 3D fusion of cine and late-enhanced cardiac magnetic resonance images, in: 2012 9th IEEE International Symposium on Biomedical Imaging (ISBI), IEEE, 2012, pp. 286–289.

[12] P.J. Slomka, D. Fieno, A. Ramesh, V. Goyal, H. Nishina, L.E. Thompson, R. Saouaf, D.S. Berman, G. Germano, Patient motion correction for multiplanar, multi-breath-hold cardiac cine MR imaging, J. Magn. Reson. Imaging 25 (5) (2007) 965–973.

[13] C. Swingen, R.T. Seethamraju, M. Jerosch-Herold, An approach to the three-dimensional display of left ventricular function and viability using MRI, Int. J. Cardiovasc. Imaging 19 (4) (2003) 325–336.

[14] A. Elen, J. Hermans, H. Hermans, F. Maes, P. Suetens, A 3D+ time spatio-temporal model for joint segmentation and registration of sparse cardiac cine MR image stacks, in: Statistical Atlases and Computational Models of the Heart. Imaging and Modelling Challenges, 2012, pp. 198–206.

[15] A. Hennemuth, A. Seeger, O. Friman, S. Miller, B. Klumpp, S. Oeltze, H.-O. Peitgen, A comprehensive approach to the analysis of contrast enhanced cardiac MR images, IEEE Trans. Med. Imaging 27 (11) (2008) 1592–1610.

[16] O. Camara, E. Oubel, G. Piella, S. Balocco, M. De Craene, A. Frangi, Multi-sequence registration of cine, tagged and delay-enhancement MRI with shift correction and steerable pyramid-based detagging, in: Functional Imaging and Modeling of the Heart, 2009, pp. 330–338.

[17] W. Shi, X. Zhuang, H. Wang, S. Duckett, D.V. Luong, C. Tobon-Gomez, K. Tung, P.J. Edwards, K.S. Rhode, R.S. Razavi, et al., A comprehensive cardiac motion estimation framework using both untagged and 3-D tagged MR images based on nonrigid registration, IEEE Trans. Med. Imaging 31 (6) (2012) 1263–1275.

[18] J. Ector, S. De Buck, J. Adams, S. Dymarkowski, J. Bogaert, F. Maes, H. Heidbüchel, Cardiac three-dimensional magnetic resonance imaging and fluoroscopy merging a new approach for electroanatomic mapping to assist catheter ablation, Circulation 112 (24) (2005) 3769–3776.

[19] S.N. Gupta, M. Solaiyappan, G.M. Beache, A.E. Arai, T.K. Foo, Fast method for correcting image misregistration due to organ motion in time-series MRI data, Magn. Reson. Med. 49 (3) (2003) 506–514.

[20] J. Lötjönen, M. Pollari, S. Kivistö, K. Lauerma, Correction of motion artifacts from cardiac cine magnetic resonance images, Acad. Radiol. 12 (10) (2005) 1273–1284.

[21] J. Barajas, K.L. Caballero, J.G. Barnés, F. Carreras, S. Pujadas, P. Radeva, Correction of misalignment artifacts among 2-D cardiac MR images in 3-D space, in: 1st International Workshop on Computer Vision for Intravascular and Intracardiac Imaging, Miccai 2006, vol. 1, 2006, pp. 114–121.

[22] D. Wei, Y. Sun, S. Ong, P. Chai, L. Teo, A. Low, et al., A comprehensive 3D framework for automatic quantification of late gadolinium enhanced cardiac magnetic resonance images, IEEE Trans. Bio-med. Eng. 60 (6) (2013) 1499–1508.

[23] W. Schroeder, K. Martin, B. Lorensen, The Visualization Toolkit: An Object Oriented Approach to 3D Graphics, Kitware, Inc. Publisher, New York.

[24] M. Malaterre, et al., GDCM Reference Manual, 1st ed., http://gdcm.sourceforge.net/gdcm.pdf, 2008.

[25] L. Ibanez, W. Schroeder, L. Ng, J. Cates, The ITK Software Guide, 1st ed., Kitware, Inc., New York, NY, USA. ISBN 1-930934-10-6, http://www.itk.org/ItkSoftwareGuide.pdf, 2003.

[26] J.V. Hajnal, Medical Image Registration, CRC Press Llc., Boca Raton, FL, USA, 2001.

[27] A. Chandler, R. Pinder, T. Netsch, J. Schnabel, D. Hawkes, D. Hill, R. Razavi, Correction of misaligned slices in multi-slice MR cardiac examinations by using slice-to-volume registration, in: 3rd IEEE International Symposium on Biomedical Imaging: Nano to Macro, 2006, IEEE, 2006, pp. 474–477.

[28] N. Noble, R. Boubertakh, R. Razavi, D. Hill, Inter-breath-hold registration for the production of high resolution cardiac MR volumes, in: Medical Image Computing and Computer-Assisted Intervention—MICCAI 2005, 2005, pp. 894–901.

[29] L.G. Brown, A survey of image registration techniques, ACM Comput. Surv. 24 (4) (1992) 325–376.

[30] S. Plein, T.N. Bloomer, J.P. Ridgway, T.R. Jones, G.J. Bainbridge, M. U. Sivananthan, Steady-state free precession magnetic resonance imaging of the heart: comparison with segmented k-space gradient-echo imaging, J. Magn. Reson. Imaging 14 (3) (2001) 230–236.

[31] J.P. Earls, V.B. Ho, T.K. Foo, E. Castillo, S.D. Flamm, Cardiac MRI: recent progress and continued challenges, J. Magn. Reson. Imaging 16 (2) (2002) 111–127.

[32] R.Y. Kwong, Cardiovascular Magnetic Resonance Imaging, Humana Press, Totowa, NJ, 2008.

[33] J.M. Bland, D. Altman, Statistical methods for assessing agreement between two methods of clinical measurement, The Lancet 327 (8476) (1986) 307–310.

[34] L.E. Hudsmith, S.E. Petersen, J.M. Francis, M.D. Robson, S. Neubauer, Normal human left and right ventricular and left atrial dimensions using steady state free precession magnetic resonance imaging, J. Cardiovasc. Magn. Reson. 7 (5) (2005) 775–782.

[35] N.A. Matheijssen, L.H. Baur, J.H. Reiber, E.A. van der Velde, P.R. van Dijkman, R. J. van der Geest, A. de Roos, E.E. van der Wall, Assessment of left ventricular volume and mass by cine magnetic resonance imaging in patients with anterior myocardial infarction intra-observer and inter-observer variability on contour detection, Int. J. Cardiac Imaging 12 (1) (1996) 11–19.